PERGAMON

International Journal of Solids and Structures 39 (2002) 4053–4071

INTERNATIONAL JOURNAL OF SOLIDS and STRUCTURES

www.elsevier.com/locate/ijsolstr

# A constitutive model for the anisotropic elastic–plastic deformation of paper and paperboard

Qingxi S. Xia, Mary C. Boyce *, David M. Parks

*Department of Mechanical Engineering, Centre of Materials Science and Technology, Massachusetts Institute of Technology, 77 Massachusetts Avenue, Cambridge, MA 02139-4307, USA*

Received 20 June 2001; received in revised form 19 February 2002

**Abstract**

A three-dimensional, anisotropic constitutive model is presented to model the in-plane elastic–plastic deformation of paper and paperboard. The proposed initial yield surface is directly constructed from internal state variables comprising the yield strengths measured in various loading directions and the corresponding ratios of plastic strain components. An associated flow rule is used to model the plastic flow of the material. Anisotropic strain hardening of yield strengths is introduced to model the evolution in the yield surface with strain. A procedure for identifying the needed material properties is provided. The constitutive model is found to capture major features of the highly anisotropic elastic–plastic behavior of paper and paperboard. Furthermore, with material properties fitted to experimental data in one set of loading directions, the model predicts the behavior of other loading states well. © 2002 Published by Elsevier Science Ltd.

*Keywords:* Paper; Paperboard; Plasticity; Yield; Yield surface; Constitutive behavior; Anisotropic

## 1. Introduction

Paper and paperboard are two of the most commonly utilized materials in nearly every industry. Paper is formed by draining a suspension of fibers in a fluid through a filter screen to form a sheet of pulp fibers. Paperboard is in general composed of several pulp fiber sheets bonded by starch or adhesive material, and is usually a multi-layered structure. Schematics of typical paper and paperboard macrostructure and microstructure are shown in Fig. 1, which also depicts the common nomenclature for the three orthogonal directions of paper and paperboard. ''MD'' refers to the machine (rolling) direction, and ''CD'' refers to the cross or transverse direction. The machine and cross directions form the plane of the structure, and ZD refers to the out-of-plane (or through-thickness) direction. Due to the continuous nature of the papermaking process, fibers are primarily oriented in the plane; furthermore, within the plane, fibers are more highly oriented in the MD than the CD. In this paper, to simplify notation, the 1-direction is used to represent the MD, the 2-direction for ZD and the 3-direction for CD.

* Corresponding author. Tel.: +1-617-253-2342; fax: +1-617-258-8742.
*E-mail address:* mcboyce@mit.edu (M.C. Boyce).

0020-7683/02/$ - see front matter © 2002 Published by Elsevier Science Ltd.
PII: S0020-7683(02)00238-X

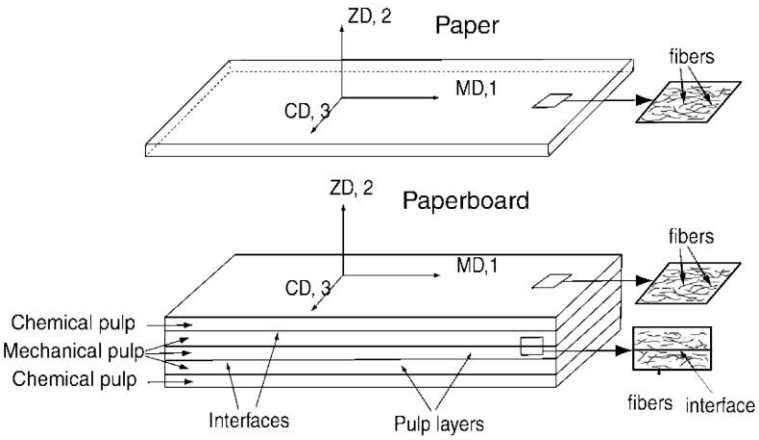


Fig. 1. Schematics of paper and paperboard macrostructure and microstructure.

The preferential fiber orientation results in highly anisotropic mechanical behavior, including anisotropic elasticity, initial yielding, strain hardening and tensile failure strength:

- Anisotropic elastic constants for paper and paperboard have been measured by several investigators (e.g., Mann et al., 1981; Castegnade et al., 1989; Persson, 1991; Koubaa and Koran, 1995). Their data show that the through-thickness moduli are at least two orders of magnitude less than the in-plane moduli. In-plane data of Persson (1991) and Stenberg et al. (2001a) show that moduli in the MD are 2–4 times greater than those of the CD.
- Persson's (1991) data on paperboard also shows that the initial yield strength (∼proportional limit) in the through-thickness direction is two orders of magnitude lower than the in-plane initial yield strength values. Stenberg's data (Stenberg et al. (2001a,b); Stenberg, 2001) on multi-layer paperboard and single-layer pulp shows similar results. Within the plane, these data show that the initial yield strength of paper and paperboard in the MD is typically greater than that in the CD by a factor of 2–4. Stenberg's data (Stenberg, 2001) also show an asymmetry in the initial yield strength for in-plane tension and compression in both the machine and cross directions.
- The in-plane tensile stress–strain curves of Persson (1991) and Stenberg (2001) show substantial strain hardening in which the yield strength increased by more than a factor of two after a strain of less than 5%. The in-plane strain hardening is also highly anisotropic. The percentage strain hardening achieved in MD tension is greater than that obtained in CD tension.
- The Persson (1991) and Stenberg (2001) data also show that the in-plane tensile failure strength in the MD is greater than that of the CD by a factor of 2–4.
- Biaxial failure stress loci (Gunderson, 1983; deRuvo et al., 1980; Fellers et al., 1981) show substantially different failure strengths in machine and cross directions. These data also show that failure tends to be dominated by one or the other of these two directions when subjected to combined loading in both directions.

Some material models have been proposed to describe the mechanical behavior of paperboard. These models fall into roughly three categories: network models, laminate models, and anisotropic models of the yield surface and/or the failure surface.

Perkins and Sinha (1992) and Sinha and Perkins (1995) described a micromechanically based network model for the in-plane constitutive behavior of paper. A meso-element was constructed to represent the

microstructure of the fibrous paper network. The mechanical response of the meso-element depends on the fiber properties and properties of the inter-fiber bonds. They found the inelastic behavior of the inter-fiber bonds to play a crucial role in the overall in-plane inelastic behavior of paper. Stahl and Cramer (1998) also developed a network model for low density fibrous composites. Network models can incorporate microlevel mechanisms, such as inter-fiber interaction and bonding. While these models begin to elucidate the underlying mechanisms of deformation, they do not provide a continuum-level description of paper or paperboard.

Page and Schulgasser (1989) and Schulgasser and Page (1988) developed models of paperboard based on classical laminate theory. While this type of model can predict the elastic response well, it was not extended to capture the anisotropic yielding and subsequent strain hardening response.

Gunderson (1983), Gunderson et al. (1986), deRuvo et al. (1980) and Fellers et al. (1981) each used the Tsai–Wu quadratic yield condition to model the failure loci they obtained experimentally. The quadratic nature of this type of model has many shortcomings when applied to paper and paperboard. Experimental data showed the biaxial failure locus to be distinctly non-quadratic. Arramon et al. (2000) developed a multidimensional anisotropic strength criterion based on Kelvin modes that captures the non-quadratic failure envelope. They applied the model to form a strength envelope for paperboard by constructing tensile and compressive modal bounds. However, these efforts only acted to study final failure and did not attempt to study initiation of yield or subsequent strain hardening.

In this research, a general three-dimensional constitutive model of the anisotropic elastic–plastic behavior of paper and paperboard is proposed. The initial elastic behavior is modelled to be linear and orthotropic. The onset of plastic flow is captured by a non-quadratic yield surface. The yield surface is taken to evolve anisotropically with a scalar measure of plastic strain, with plastic flow modelled using an associated flow rule. The model is detailed in the following sections, and numerical results are compared to experimental data.

## 2. Experimentally observed behavior

### 2.1. Elastic–plastic behavior of TRIPLEX paperboard

Depending on fiber type, fiber density and the chemical/mechanical treatment, the elastic–plastic behavior of different types of paper and paperboard differs in detail. However, general characteristics of the response remain similar. In this contribution, the anisotropic elastic–plastic behavior of paper and paperboard is illustrated using TRIPLEX™ [1] paperboard as an exemplar material. TRIPLEX™ is a five-layer paperboard: the three-layer core is constructed from mechanically processed softwood pulp (commonly referred to as "mechanical" pulp), and two outer layers (sandwiching the core) are constructed from bleached kraft pulp (commonly referred to as "chemical" pulp). Stenberg et al. (2001a,b) and Stenberg (2001) conducted an extensive experimental investigation documenting the stress–strain behavior of TRIPLEX™. Note that the outer chemical pulp layers are typically stiffer and stronger than the inner mechanical layers; however, these layers cannot be separately produced for individual evaluation. Therefore, the behavior of TRIPLEX™ material will be presented in terms of its effective composite behavior. In principle, testing and modeling can be applied separately for each distinct paper lamina. The experimental results of Stenberg et al. (2001a,b) and Stenberg (2001) are reviewed below.

[1] TRIPLEX™ is a trademark of STORA-ENSO, Finland and Sweden.

*2.1.1. In-plane behavior*

The in-plane uniaxial tensile stress–strain curves for the MD, the CD and an orientation 45° from the MD are plotted together in Fig. 2. These stress–strain curves clearly depict the anisotropic in-plane elastic, initial yield and strain hardening behavior. There is a factor of 2–3 difference in the modulus and initial yield strength between MD and CD. Hardening achieved in MD (flow strength increases by 300% over a strain of 2%) is higher than that in CD (flow strength increases by 200% over a strain of 5%). MD–CD shear properties are deduced from the 45° test result.

In-plane lateral strain (CD) vs. axial strain data for MD-tension and similar data for CD-tension were also recorded by Stenberg (2001), corresponding to their in-plane stress strain curves. Upon subtracting the respective elastic strain components, the lateral plastic strains for both the MD and CD tension cases are computed and shown vs. the respective axial plastic strains in Fig. 3. These two curves indicate that for both test orientations, the ratio between lateral plastic strain and axial plastic strain is nearly constant until final fracture. This data provides information for later construction of the plastic flow rule.

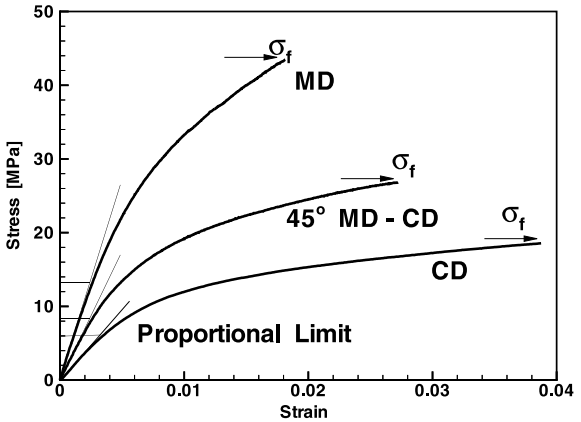


Fig. 2. TRIPLEX™ in-plane tensile stress–strain curves (Stenberg, 2001).

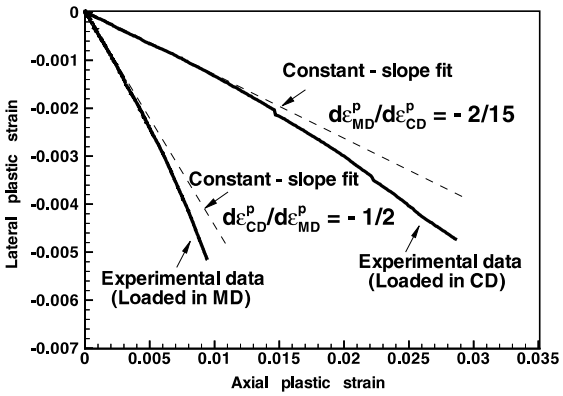


Fig. 3. Lateral plastic strain vs. axial plastic strain curves for tensile loading in the MD and CD directions (Stenberg, 2001).

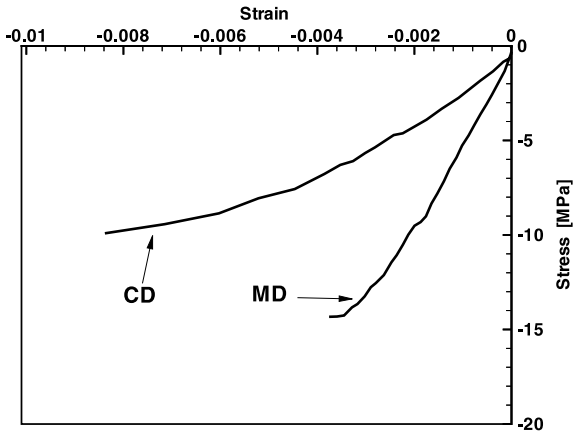


Fig. 4. In-plane compression stress–strain curves for MD and CD directions (Stenberg, 2001).

Tensile loading/unloading/reloading data (Persson, 1991; Stenberg, 2001) show that after various amounts of plastic strain, upon unloading, the elastic tensile modulus is nearly unaffected by plastic strain, consistent with traditional models of elasto-plasticity.

Fig. 4 shows the in-plane compression stress–strain curves for the MD and CD directions. Note that global specimen buckling was constrained in these tests. These data show that compressive yield is anisotropic. Furthermore, a comparison of Figs. 2 and 4 shows a yield strength difference between tension and compression, with the compressive yield strengths being smaller than those in tension by 65% and 25%, for MD and CD, respectively.

The anisotropic in-plane elastic–plastic properties obtained from these tests are summarized in Table 1.

### 2.1.2. Out-of-plane behavior

Stenberg et al. (2001a,b) experimentally obtained the out-of-plane stress–strain behavior of paperboard using a modified Arcan design (Arcan et al., 1978). Nominal stress–strain curves were obtained for TRIPLEX™ under various through-thickness loading conditions.

Representative ZD tensile and through-thickness shear (ZD–MD) stress–strain curves obtained by Stenberg et al. (2001a,b) are shown in Fig. 5. The stress measure is force per unit initial cross-sectional area; the $x$-ordinate is the nominal strain, defined as the relative normal/shear separation of the top and bottom surfaces of the laminate, divided by the initial laminate thickness. In the tensile curve, at the earliest stage of deformation, the stress increases linearly with strain, exhibiting a composite modulus of $E^0_{ZD} = 18.0$ MPa. The stress–strain relation shows a small amount of pre-peak non-linearity before reaching a peak stress of 0.4 MPa. After the peak, the stress–strain curve exhibits pronounced softening. Features similar to those of the through-thickness tensile curve are observed for the through-thickness shear curve. The composite

Table 1
Experimental results of uniaxial tensile tests (Stenberg, 2001)

| | Elastic modulus (GPa) | Poisson's ratio | Tensile yield strength (MPa) | Plastic strain ratio, $d\epsilon^p_\perp/d\epsilon^p_\parallel$ | Compressive yield strength (MPa) |
|---|---|---|---|---|---|
| MD | 5.6 | 0.37 | 12.0 | −0.5 | 7.3 |
| CD | 2.0 | 0.12 | 6.5 | −0.133 | 5.0 |
| 45° | 4.1 | | 8.0 | | |

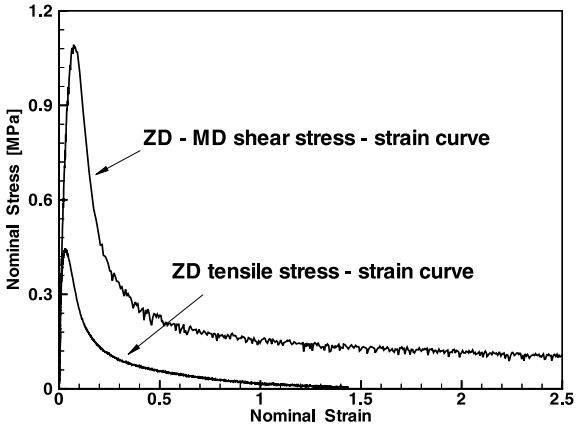


Fig. 5. Through-thickness ZD tension/shear stress–strain curves (Stenberg et al. (2001a,b)).

Table 2
Elastic out-of-plane properties (Stenberg et al. (2001a,b))

| Elastic modulus $E^0_{ZD}$ (MPa) | Poisson's ratio $v_{21}$ | Poisson's ratio $v_{23}$ | Shear modulus $G_{12}$ (MPa) | Shear modulus $G_{23}$ (MPa) | Stiffening constant $a$ |
|---|---|---|---|---|---|
| 18.0 | −0.0055 | −0.0035 | 34.0 | 26.0 | 5.4 |

transverse shear modulus is observed to be $G_{12} = 34$ MPa, and the peak shear stress is 1.1 MPa. The through-thickness ZD–CD shear stress–strain curve shows similar features.

Through-thickness tensile/shear testing conducted within a scanning electron microscope (Dunn, 2000) on the same material reveals the nucleation of multiple inter-laminar microcracks near the peak stress, followed by their growth and coalescence, resulting in the observed softening. Similar results have been obtained for tests involving combined through-thickness tension and shear (Dunn, 2000; Stenberg et al. (2001a,b)). Therefore, the observed peak stress and subsequent softening for through-thickness loading are due to delamination of the paperboard and will not be further considered here. This inelastic through-thickness behavior is modelled in a separate related study (Xia et al., in preparation). It is also observed that the amount of lateral (in-plane) strain generated during the through-thickness tensile loading is negligible, indicating that Poisson's ratios $v_{21}$ and $v_{23}$ are close to zero.

Through-thickness compression loading/unloading stress–strain curves were also obtained by Stenberg (2001). Up to a nominal compressive strain of 3%, the compressive stress increases linearly with strain. With larger strains, the stress starts to increase exponentially with strain. The data also show that only a small amount of permanent deformation is remained after unloading from a peak strain level of more than 20%, indicating non-linear elastic ZD compressive behavior up to moderately large strains. These observations of through-thickness compressive behavior will be incorporated into the modeling work.

The anisotropic linear elastic out-of-plane properties are summarized in Table 2.

## 3. Constitutive model

A three-dimensional, finite deformation constitutive model for paper and paperboard pulp layers is proposed. The model will take the in-plane behavior to be elastic–plastic and the out-of-plane behavior to be elastic. Due to the assumption of elastic out-of-plane behavior, the application of the model alone will be limited to predominant in-plane loading. However, when the model is combined with interlaminar deco-

hesion models (Xia et al., in preparation), a general-purpose tool is achieved for modeling behavior under significant out-of-plane loading, such as occurs during converting processes and the in-service behavior of a broad class of paper and paperboard products.

### 3.1. Stress–strain relationship

First, the total deformation gradient $\boldsymbol{F}$ at a material point within a lamina is multiplicatively decomposed into an elastic part and a plastic part:

$$\boldsymbol{F} = \boldsymbol{F}^{\mathrm{e}}\boldsymbol{F}^{\mathrm{p}}, \tag{1}$$

where $\boldsymbol{F}^{\mathrm{p}}$ represents the accumulation of inelastic deformation. Although the maximum in-plane strain level in traditional applications of paper sheets is small, we adopt the present finite deformation formulation so that the model can be easily applied to applications such as paperboard converting processes, which generally involve finite rotations of paperboard layers and may exhibit moderately large, but highly localized in-plane strains. The evolution of $\boldsymbol{F}^{\mathrm{p}}$ is given by

$$\dot{\boldsymbol{F}}^{\mathrm{p}} = \boldsymbol{L}^{\mathrm{p}}\boldsymbol{F}^{\mathrm{p}}, \tag{2}$$

where $\boldsymbol{L}^{\mathrm{p}}$ is the plastic velocity gradient, which will be defined by the flow rule. The elastic strain is obtained by using the elastic Green strain measure:

$$\boldsymbol{E}^{\mathrm{e}} = \tfrac{1}{2}\left[\boldsymbol{F}^{\mathrm{e}\mathrm{T}}\boldsymbol{F}^{\mathrm{e}} - \boldsymbol{I}\right], \tag{3}$$

where $\boldsymbol{I}$ is the second-order identity tensor. The second Piola–Kirchoff stress measure, $\overline{\boldsymbol{T}}$, relative to the plastically deformed configuration $\boldsymbol{F}^{\mathrm{p}}$, is then calculated using the linear relationship:

$$\overline{\boldsymbol{T}} = \boldsymbol{C}[\boldsymbol{E}^{\mathrm{e}}], \tag{4}$$

where $\boldsymbol{C}$ is the fourth-order stiffness tensor, which is taken to be orthotropic. Values of the components of $\boldsymbol{C}$ are defined by the orthotropic elastic moduli. To model the through-thickness non-linear elastic compressive stress–strain relationship, the through-thickness engineering elastic constant, $E_{\mathrm{ZD}}$, is taken to be an exponential function of the ZD strain under compression as follows:

$$E_{\mathrm{ZD}} = E^{0}_{\mathrm{ZD}}\exp(-aE^{\mathrm{e}}_{22}), \tag{5}$$

where $E^{0}_{\mathrm{ZD}}$ is the initial elastic modulus in ZD, $E^{\mathrm{e}}_{22}$ is the ZD elastic Green strain component, and $a$ is a constant determined by fitting the compressive through-thickness stress–strain curve; its value is listed in Table 2. The stiffness tensor $\boldsymbol{C}$ under ZD compression is in turn determined assuming constant Poisson's ratios. The Cauchy stress, $\boldsymbol{T}$, is calculated from its relation to the second Piola–Kirchoff stress by

$$\overline{\boldsymbol{T}} = (\det \boldsymbol{F}^{\mathrm{e}})\boldsymbol{F}^{\mathrm{e}-1}\boldsymbol{T}\boldsymbol{F}^{\mathrm{e}-\mathrm{T}}. \tag{6}$$

### 3.2. Yield condition

The through-thickness strengths (tensile, compressive, shear) of paper and paperboard materials are typically two orders of magnitude lower than those observed in the plane. Therefore, the through-thickness stress components play little role in the inelastic deformation and failure of paperboard under in-plane loading. [2] Furthermore, from investigation of the mechanisms of deformation and failure of paperboard

[2] Under significant in-plane compression or very large through-thickness compressive strain, this may not be strictly true. However, for the present, these scenarios will not be considered further.

under through-thickness loading (when through-thickness compression is not dominant), it is clear that the majority of through-thickness inelastic deformation occurs in the form of interlaminar microcracking and delamination of the discrete pulp layers, as opposed to inelastic through-thickness deformation distributed quasi-homogeneously within laminae. Thus we can assume that only the in-plane stress components will drive the in-plane inelastic deformation of the pulp layers. Additionally, in classical metal plasticity and in plasticity-based models of yielding in polymers, the deviatoric stress is taken to drive yield because the underlying deformation mechanisms are governed by shear (for example, dislocation glide in crystalline metals). However, in the case of paper, there is no evidence that yield and subsequent plastic flow are driven by deviatoric stress. Micromechanically, yielding is governed by various forms of inter-fiber interactions. Based on these considerations, the total stress will be taken to drive the yield condition described in this research.

In order to experimentally define an in-plane yield surface for paper, multi-axial data is required. Although the anisotropy of the yield surface is well-recognized, due to numerous studies of the uniaxial behavior in different directions, such as that reported in Fig. 2, a literature search reveals virtually no data on the initial and evolving multi-axial yield surfaces of paper and paperboard. However, several researchers have obtained biaxial failure surfaces of paperboard under combinations of MD and CD normal stress. Fig. 6 shows a representative biaxial failure locus (deRuvo et al., 1980). Similar data have been reported in work by Fellers et al. (1981) and Gunderson (1983). One common feature observed in these failure loci is that the data points tend to form prominent sub-groups, with each sub-group lying on a nearly straight line. For example, for low, but non-zero values of MD stress, failure occurs at nearly the CD uniaxial tensile failure strength; similarly, for low, but non-zero values of CD stress, failure occurs at roughly the MD uniaxial tensile failure strength. This observation suggests that the experimental biaxial failure locus can be well captured by a set of straight lines in two-dimensional biaxial stress space and can be generalized to planes in three-dimensional space. Karafillis and Boyce (1993) and Arramon et al. (2000) developed yield surface and failure surface models, respectively, which capture this non-quadratic feature. In stress space, these lines or planes can be defined by their minimum distance to the origin, together with their corresponding normal directions. Given that a comprehensive set of experimental data is generally unavailable (and indeed, is a challenging task to obtain) to determine the full surface, we hereby assume that the yield surface exhibits the same characteristic features observed in the failure surface. Therefore, the yield surface is taken to be constructed of $N$ sub-surfaces, where $\boldsymbol{N}^K$ is the normal to the $K$th such surface, defined in the material coordinates formed by MD, CD and ZD. $S^K$ is the equivalent strength of the $K$th sub-surface, defined by the distance from the origin to each sub-surface, following its normal direction. Thus, the following form of yield criterion is proposed:

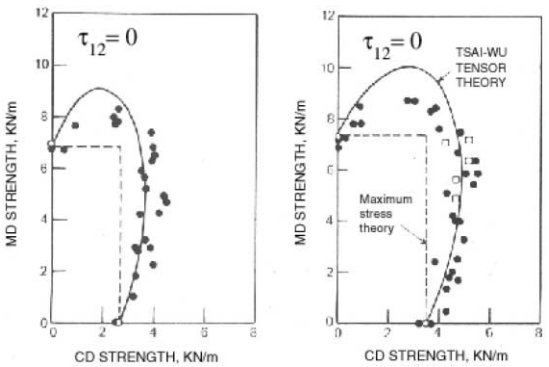


Fig. 6. Biaxial failure surfaces (deRuvo et al., 1980).

$$f(\overline{\boldsymbol{T}}, S^K) = \sum_{K=1}^{N} \left[ \frac{\chi_K \overline{\boldsymbol{T}} \cdot \boldsymbol{N}^K}{S^K} \right]^{2k} - 1, \tag{7}$$

where $\chi_K$ is the switching controller with

$$\chi_K = \begin{cases} 1; & \text{if } \overline{\boldsymbol{T}} \cdot \boldsymbol{N}^i > \boldsymbol{0}, \\ \boldsymbol{0}; & \text{otherwise}, \end{cases} \tag{8}$$

$\overline{\boldsymbol{T}}$ is the second Piola–Kirchoff stress measure relative to the $\boldsymbol{F}^{\mathrm{p}}$ configuration, and $2k$ is an even integer. $\boldsymbol{N}^K$ is the normal of the $K$th sub-surface, defined relative to the material coordinates.

A schematic of a four sub-surface system for biaxial loading, with zero in-plane shear stress, is shown in Fig. 7. The normals and corresponding sub-surface strengths are illustrated. The parameter $2k$ is taken to be equal to or larger than 4, indicating a non-quadratic yield surface. Fig. 8 shows the effect of different $2k$ values in controlling the shape of the yield surface in the biaxial stress plane for this simplified four sub-surface system. Higher $2k$-values give rise to sharper corners between adjacent sub-surfaces and reduce the curvature over increasing central portions of each sub-surface. A schematic of a six sub-surface yield surface, with non-zero in-plane shear stress $\overline{T}_{13}$, is shown in Fig. 9. This figure graphically illustrates the

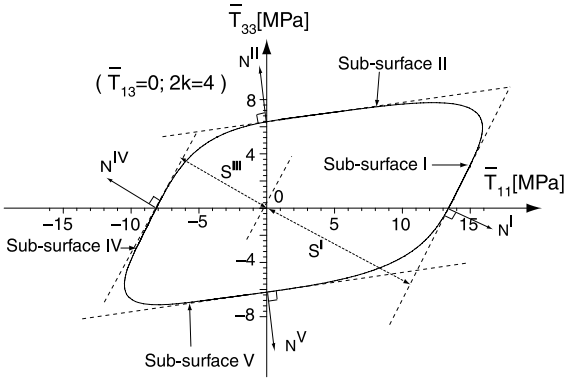


Fig. 7. Initial yield surface for biaxial normal stress loadings, showing its four sub-surfaces ($2k = 4$).

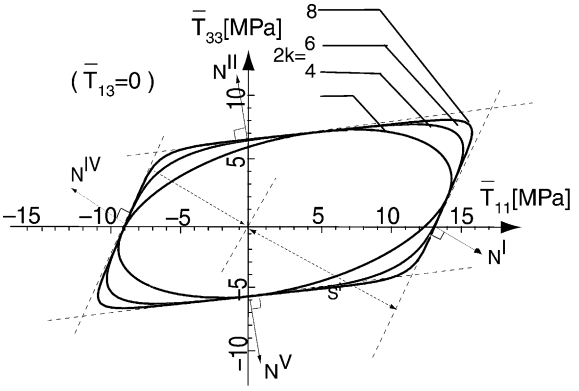


Fig. 8. Effect of constant $2k$ on the shape of yield surface.

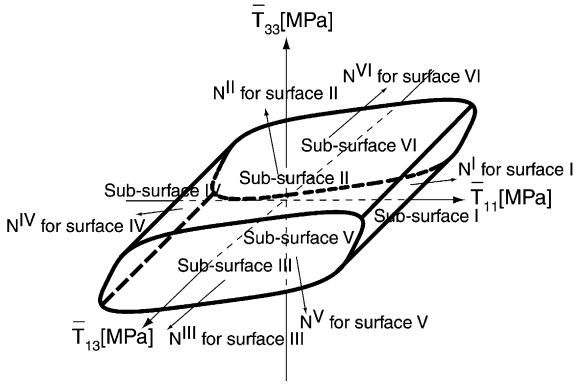


Fig. 9. Schematic of yield surface for general in-plane loading, showing six sub-surfaces.

normals and corresponding equivalent strengths of the sub-surfaces. For this yield surface, the six normals are taken to be of the following form:

$$\boldsymbol{N}^K = \sum_{i,j=1}^{3} N_{ij}^K \boldsymbol{e}_i \otimes \boldsymbol{e}_j, \quad K = \mathrm{I}, \ldots, \mathrm{VI} \tag{9}$$

and

$$N_{ji}^K = N_{ij}^K, \quad K = \mathrm{I}, \ldots, \mathrm{VI}, \tag{10}$$

where $\boldsymbol{e}_i$ are the basis vectors for the material coordinates formed by the MD, CD and ZD. Here, the sub-surface normal index $K$ ranges over the six Roman numerals I–VI.

Because out-of-plane stress components are assumed to have no effect on the plastic deformation within a lamina, components of $\boldsymbol{N}^K$ involving the 2-direction (i.e., the ZD direction) are set to be zero. This results in elastic through-thickness behavior, as proposed. Determination of each non-zero entry of these matrices will be discussed in Section 3.3.

### 3.3. Flow rule

The plastic flow rule is defined as

$$\boldsymbol{L}^{\mathrm{p}} = \boldsymbol{D}^{\mathrm{p}} = \dot{\bar{\gamma}} \boldsymbol{K}, \tag{11}$$

where $\boldsymbol{L}^{\mathrm{p}}$ is the plastic flow rate and $\boldsymbol{D}^{\mathrm{p}}$ is the symmetric part of $\boldsymbol{L}^{\mathrm{p}}$. For paper and paperboard, the in-plane plastic strains (even at failure) are small; therefore we take the skew part of $\boldsymbol{L}^{\mathrm{p}}$ to vanish, or $\boldsymbol{W}^{\mathrm{p}} = 0$, as a simplification. $\boldsymbol{K}$ is the flow direction, and $\dot{\bar{\gamma}}$ is the magnitude of the plastic stretching rate. $\boldsymbol{K}$ is a second-order tensor with unit magnitude:

$$\boldsymbol{K} = \widehat{\boldsymbol{K}} / \| \widehat{\boldsymbol{K}} \|, \tag{12}$$

where

$$\| \widehat{\boldsymbol{K}} \| = \sqrt{\widehat{\boldsymbol{K}} \cdot \widehat{\boldsymbol{K}}} = \sqrt{\sum_{i,j=1}^{3} \widehat{K}_{ij} \widehat{K}_{ij}}. \tag{13}$$

In Fig. 3, the in-plane lateral plastic strain vs. axial plastic strain data showed that the ratio between these two plastic strain components is nearly constant for both the MD and CD simple tension cases. These ratios are taken to define the normal directions of the two respective sub-surfaces of the tensile quadrant of the biaxial yield surface, in the absence of shear stress. Thus, the plastic flow of the material is taken to follow an associated flow rule:

$$\widehat{\boldsymbol{K}} = \frac{\partial f}{\partial \overline{\boldsymbol{T}}}. \tag{14}$$

With the yield condition defined in Eq. (7), $\widehat{\boldsymbol{K}}$ can be further calculated as

$$\widehat{\boldsymbol{K}} = \frac{\partial f}{\partial \overline{\boldsymbol{T}}} = \sum_{K=1}^{N} 2k\Lambda_K^{2k-1} \frac{\chi_K \boldsymbol{N}^K}{S^K}, \tag{15}$$

where

$$\Lambda_K = \frac{\overline{\boldsymbol{T}} \cdot \boldsymbol{N}^K}{S^K}. \tag{16}$$

For the six sub-surface yield surface shown in Fig. 9, assuming an associated flow rule, the sub-surface normals $\boldsymbol{N}^K$, $K = \mathrm{I}, \ldots, \mathrm{VI}$ are defined using the corresponding plastic strain ratios. For example, for sub-surface I (one) in Fig. 9, the plastic strain ratio from the MD simple tension test is nearly constant at $-0.5$. The two non-zero components of $\boldsymbol{N}^{\mathrm{I}}$ are then determined by solving the following two equations:

$$\frac{N_{33}^{\mathrm{I}}}{N_{11}^{\mathrm{I}}} = -0.5 \tag{17}$$

and (to make a unit normal)

$$(N_{11}^{\mathrm{I}})^2 + (N_{33}^{\mathrm{I}})^2 = 1, \tag{18}$$

which gives $N_{11}^{\mathrm{I}} = 2/\sqrt{5}$ and $N_{33}^{\mathrm{I}} = -1/\sqrt{5}$. Similarly, the plastic strain ratio from the CD simple tension test is nearly constant at $-2/15$, giving $N_{11}^{\mathrm{II}} = -2/\sqrt{229}$ and $N_{33}^{\mathrm{II}} = 15/\sqrt{229}$. With appropriate experimental data, similar calculations can determine the normals of each of the sub-surfaces. However, currently, there is no experimental data for the plastic strain ratios for compression in either the machine or cross directions. For the four sub-surface biaxial yield surface shown in Fig. 7, the normals for the two sub-surfaces in the compressive quadrants, IV and V, are assumed to have normal directions parallel to those of corresponding tensile sub-surfaces, I and II, respectively, as seen in the figure, but with generally differing strength levels. For the normal of the sub-surface representing yielding under positive pure shear stress ($\overline{T}_{13} = \overline{T}_{31} \neq 0$; $\overline{T}_{ij} = 0$ otherwise), the two non-zero components are $N_{13}^{\mathrm{III}}$ and $N_{31}^{\mathrm{III}}$. Due to the symmetry of shear stress,

$$N_{13}^{\mathrm{III}} = N_{31}^{\mathrm{III}} \tag{19}$$

and

$$(N_{13}^{\mathrm{III}})^2 + (N_{31}^{\mathrm{III}})^2 = 1. \tag{20}$$

Thus we have $N_{13}^{\mathrm{III}} = N_{31}^{\mathrm{III}} = \sqrt{2}/2$, and the normal of the other sub-surface representing yielding under negative pure shear stresses is taken to be $\boldsymbol{N}^{\mathrm{VI}} = -\boldsymbol{N}^{\mathrm{III}}$. In summary, the components of the normals for the six sub-surfaces determined in the material coordinates are given in Table 3.

### 3.4. Strain hardening functions

To capture the anisotropic strain hardening observed for the in-plane behavior, the equivalent strengths, $S^K$, of each sub-surface are taken to evolve with the accumulated equivalent plastic strain, i.e.

Table 3
Non-zero components of the sub-surface normals used in modeling TRIPLEX™, expressed in the material coordinates

| $K$ | $N_{11}^K$ | $N_{33}^K$ | $N_{13}^K$ |
|---|---|---|---|
| I | $2/\sqrt{5}$ | $-1/\sqrt{5}$ | 0.0 |
| II | $-2/\sqrt{229}$ | $15/\sqrt{229}$ | 0.0 |
| III | 0.0 | 0.0 | $\sqrt{2}/2$ |
| IV | $-2/\sqrt{5}$ | $1/\sqrt{5}$ | 0.0 |
| V | $2/\sqrt{229}$ | $-15/\sqrt{229}$ | 0.0 |
| VI | 0.0 | 0.0 | $-\sqrt{2}/2$ |

$$S^K = S^K(\bar{\gamma}), \tag{21}$$

where $\bar{\gamma} = \int \dot{\bar{\gamma}} \mathrm{d}t$ is the equivalent plastic strain. Fig. 10 shows schematically how the shape of a biaxial yield surface evolves with increasing equivalent plastic strain for the case of zero in-plane shear stress. For the yield surface, the $S^K$ values, $K = \mathrm{I}$, II, IV and V, are directly related to the uniaxial yield strength of the material for MD/CD tension and compression and the corresponding plastic strain ratios (see Appendix A). The equivalent yield strengths for the two pure shear sub-surfaces are taken to be equal, $S^{\mathrm{III}} = S^{\mathrm{VI}}$, and are related to the in-plane MD–CD shear strength.

In this research, anisotropic strain hardening is modelled by taking the $S^K$ to depend on the amount of accumulated plastic strain as follows:

$$\begin{aligned}
S^{\mathrm{I}} &= S_0^{\mathrm{I}} + A_1 \tanh(B_1\bar{\gamma}) + C_1\bar{\gamma},\\
S^{\mathrm{II}} &= S_0^{\mathrm{II}} + A_2 \tanh(B_2\bar{\gamma}) + C_2\bar{\gamma},\\
S^{\mathrm{III}} &= S_0^{\mathrm{III}} + A_3 \tanh(B_3\bar{\gamma}) + C_3\bar{\gamma},\\
S^{\mathrm{IV}} &= S_0^{\mathrm{IV}} + A_4 \tanh(B_4\bar{\gamma}) + C_4\bar{\gamma},\\
S^{\mathrm{V}} &= S_0^{\mathrm{V}} + A_5 \tanh(B_5\bar{\gamma}) + C_5\bar{\gamma},\\
S^{\mathrm{VI}} &= S^{\mathrm{III}},
\end{aligned} \tag{22}$$

where $S_0^{\mathrm{I}}$, $S_0^{\mathrm{II}}$, $S_0^{\mathrm{III}}$, $S_0^{\mathrm{IV}}$ and $S_0^{\mathrm{V}}$ are the initial equivalent yield strength for sub-surface I–V, respectively, $A_i$, $B_i$, $C_i$, $i = 1, \ldots, 5$ are hardening constants.

The constants are determined by fitting the experimental stress–strain curves, as discussed further in Appendix A.

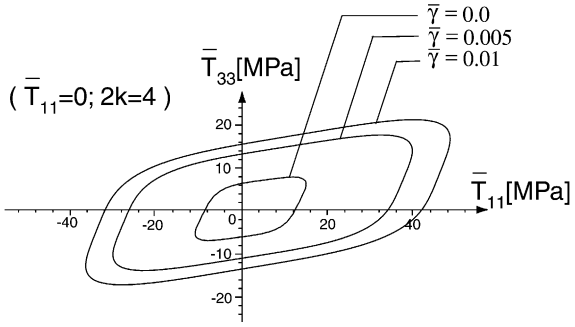


Fig. 10. Hardening of yield surface ($2k = 4$).

## 4. Simulation and results

The constitutive model described above was numerically integrated using a Newton–Raphson procedure. Several homogeneous deformations were simulated to test the model. First, simulations were conducted to verify the fit of material properties to data. Uniaxial tension data on TRIPLEX™ paperboard in the MD, CD and 45° direction were used to fit the material properties as were compression data in the MD and CD. A method for fitting model properties to data is given in Appendix A. After the model properties were calibrated with the MD, CD and 45° data, these parameters were used to predict the stress–strain behavior during tensile loading in directions 22.5° and 67° off-axis of the MD and were compared to experimental data. It is worth noting that the experimental stress–strain and lateral strain vs. axial strain curves being fitted are curves obtained from experiments conducted on TRIPLEX™, which is a five-layer paperboard. While the constitutive model can be applied separately to each layer of the paperboard, here the effective properties for the five-layer laminate as a single entity are obtained through data-fitting, and therefore represent the averaged value for the whole laminate.

Comparisons of the experimental and the simulated stress–strain curves for uniaxial MD, CD and 45° tension are shown in Fig. 11. Fig. 12 shows the corresponding comparison of experimental and simulated lateral strain vs. axial strain curve for the MD and CD. These results demonstrate that the proposed model can capture the elastic–plastic behavior of the paperboard over the full range of strain. It is also seen that an associated flow rule with a simple constant normal direction for the sub-surface captures the lateral strain vs. axial strain curves well. If second-order accuracy is needed to capture the lateral strain vs. axial strain curve, the sub-surface normals, $\boldsymbol{N}^K$ could perhaps be taken to evolve with plastic straining. The CD result, together with the MD result, demonstrates the anisotropic capability of the proposed model.

Compression simulations are also conducted. Fig. 13 shows the comparison of the experimental and the simulated stress–strain curve for uniaxial MD and CD compression. These results show that the model is capable of capturing the asymmetric tension and compression yielding and hardening behavior.

By fitting these experimental curves, the properties needed in the model were determined. Some of material properties have been listed in Sections 3.4. The remaining ones are listed in Appendix A. The final set of parameters describing the initial yield surface and the hardening of the yield surface used in the simulations were shown in Figs. 7 and 10. It is also worth noting that the specimen failed under less than 0.4% of total compressive MD strain. Thus the compressive quadrants of the hardened yield surfaces shown in Fig. 10 are of less practical meaning when plastic strain is larger than the strain at which the specimen failed.

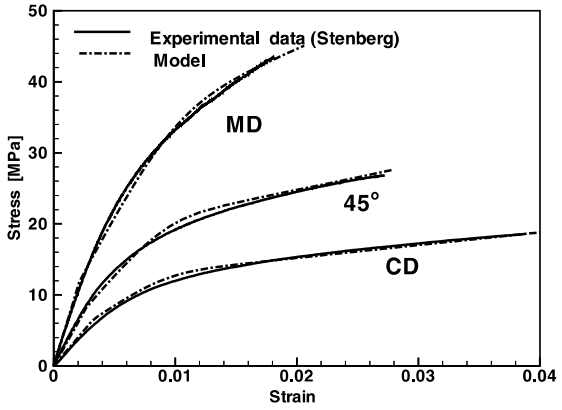


Fig. 11. Comparison of experimental and simulated stress–strain curves for uniaxial MD, CD and 45° tension.

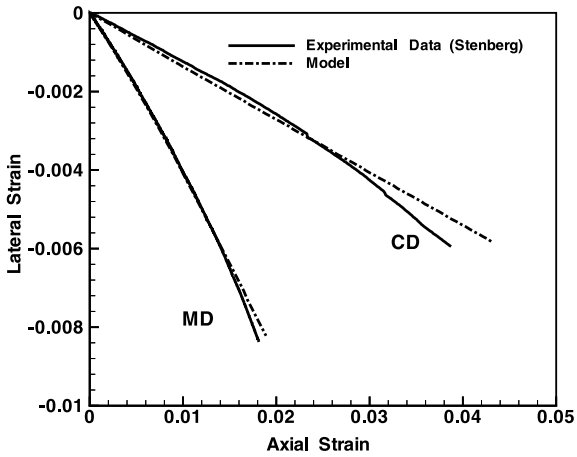


Fig. 12. Comparison of experimental and simulated lateral strain vs. axial strain curves for uniaxial MD and CD tension.

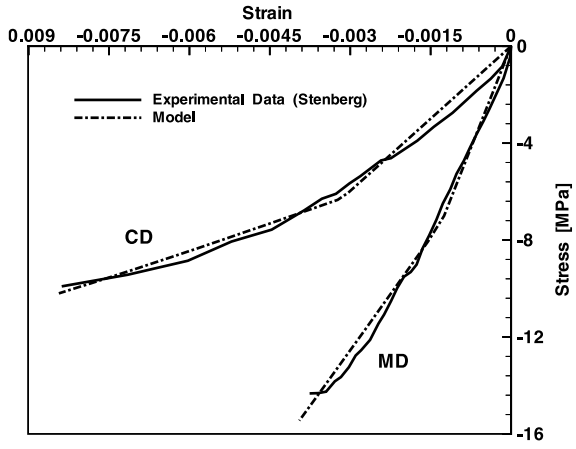


Fig. 13. Comparison of experimental and simulated stress–strain curves for uniaxial MD and CD compression.

With the material properties obtained from fitting the MD, CD and 45° data, two simulations were then conducted to test the predictive capability of the model. The stress–strain behavior subjected to tensile loading in two off-axis directions, 22.5° from the MD and 67° from the MD, are simulated. Fig. 14 compares the experimental and the simulated stress–strain curves in these two loading directions. The stress–strain curves predicted by the model are in good agreement with the corresponding experimental curves, showing that the model is capable of providing good predictions to the in-plane stress–strain behavior.

## 5. Discussion and future work

This work presented a finite deformation elastic–plastic constitutive model for in-plane behavior of paper and paperboard. The anisotropic elasticity is modelled using orthotropic linear elasticity, albeit generalized to connect the work-conjugate stress and strain measures $\overline{\boldsymbol{T}}$ and $\boldsymbol{E}^{e}$. The initial anisotropic yield

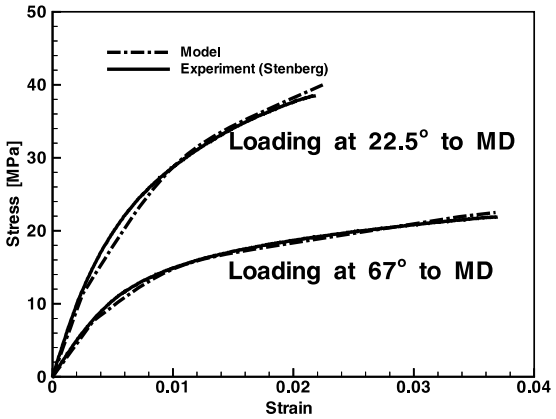


Fig. 14. Comparison of experimental and predicted stress–strain curves for tensile loading in off-axis directions 22.5° and 67° from the MD direction.

behavior is modelled by an initial yield surface constructed from sub-surfaces defined by the measured initial yield strengths and plastic strain ratios in various loading conditions. The strength of each sub-surface is taken to harden with respect to the equivalent plastic strain, thus providing anisotropic strain hardening of the yield surface. The material parameters needed by the model are obtained by fitting uni-axial stress–strain and lateral strain vs. axial strain data. With the fitted parameters, the model was shown to be predictive of other in-plane stress–strain behavior.

The proposed model can be applied to simulate a wide range of in-plane problems for paper and paperboard such as the behavior under bending or inhomogeneous, multiaxial in-plane loading. With more experimental information (e.g., off-axis stress–strain curves with corresponding lateral strain vs. axial strain curves), the yield surface and, in turn, the flow rule can be easily refined to provide even more accurate modeling of the behavior of paper or paperboard layer by incorporating more sub-surfaces. Furthermore, the proposed constitutive model, together with modeling of the through-thickness tensile and shear behavior, enables the simulation of complex loading conditions such as those that occur during various converting processes as well as drop-loading conditions of paperboard products.

## Acknowledgements

Financial support for this work provided by STFI, Stora–Enso, Tetra Pak and Assi Domän is gratefully acknowledged. Part of the experimental data used in this research was obtained from our colleagues from STFI and KTH, Mr. Niclas Stenberg, Prof. Christer Fellers and Prof. Sören Östlund. Their help and comments on this research work are gratefully acknowledged. The authors thank two former MIT students, Heather Dunn and Alexis Smith, for conducting SEM testing on paperboard which provided important insights to this modeling work. The authors would also like to acknowledge many stimulating discussions with the project steering committee including representatives from STFI, Stora–Enso, Tetra Pak, Assi Domän, and HKS, Inc.

## Appendix A

In this appendix, we summarize the definition of the material properties (Table 4) and the method to obtain them from experimental data. The yield surface is comprised of six sub-surfaces as shown in Fig. 9.

Table 4
Definition of properties

| Notes | Properties | Definition |
|---|---|---|
| Elasticity (see Tables 1 and 2) | $E_{MD}$ | Young's modulus in MD direction |
| | $E_{CD}$ | Young's modulus in CD direction |
| | $E_{ZD}$ | Young's modulus in ZD direction |
| | $\nu_{12}$ | Poisson's ratio between MD and ZD directions |
| | $\nu_{13}$ | Poisson's ratio between MD and CD directions |
| | $\nu_{23}$ | Poisson's ratio between ZD and CD directions |
| | $G_{12}$ | Shear modulus in the MD–ZD plane |
| | $G_{13}$ | Shear modulus in the MD–CD plane |
| | $G_{23}$ | Shear modulus in the CD–ZD plane |
| Initial value of sub-surface strengths (Table 5) | $S_0^{I}$ | Initial equivalent yield strength of sub-surface I |
| | $S_0^{II}$ | Initial equivalent yield strength of sub-surface II |
| | $S_0^{III}$ | Initial equivalent yield strength of sub-surface III |
| | $S_0^{IV}$ | Initial equivalent yield strength of sub-surface IV |
| | $S_0^{V}$ | Initial equivalent yield strength of sub-surface V |
| | $S_0^{VI}$ | Initial equivalent yield strength of sub-surface VI |
| Flow strength of sub-surfaces (Eq. (22)) | $S^{I}$ | Flow strength of sub-surface I |
| | $S^{II}$ | Flow strength of sub-surface II |
| | $S^{III}$ | Flow strength of sub-surface III |
| | $S^{IV}$ | Flow strength of sub-surface IV |
| | $S^{V}$ | Flow strength of sub-surface V |
| | $S^{VI}$ | Flow strength of sub-surface VI |
| Hardening constants (Table 5) | $A_i$, $i = 1,\ldots,5$ | Hardening constants in Eq. (22) |
| | $B_i$, $i = 1,\ldots,5$ | Hardening constants in Eq. (22) |
| | $C_i$, $i = 1,\ldots,5$ | Hardening constants in Eq. (22) |
| Stiffening constant (Table 2) | $a$ | Constant determining stiffening of ZD elastic modulus under compression (Eq. (5)) |

## *A.1. Definition of properties*

The elastic properties used for TRIPLEX™ were listed in Tables 1 and 2. The yield and post-yield properties are listed here in Table 5. The yield surface normals were listed in Table 3.

Table 5
In-plane plastic properties used by model for TRIPLEX™

| $S_0^{I}$ (MPa) | $S_0^{II}$ (MPa) | $S_0^{III}$ (MPa) | $S_0^{IV}$ (MPa) | $S_0^{V}$ (MPa) |
|---|---|---|---|---|
| 12.0 | 6.5 | 6.0 | 7.3 | 6.3 |
| $A_1$ (MPa) | $A_2$ (MPa) | $A_3$ (MPa) | $A_4$ (MPa) | $A_5$ (MPa) |
| 19.0 | 40.0 | 6.0 | 6.0 | 9.0 |
| $B_1$ | $B_2$ | $B_3$ | $B_4$ | $B_5$ |
| 260.0 | 160.0 | 375.0 | 160.0 | 310.0 |
| $C_1$ (MPa) | $C_2$ (MPa) | $C_3$ (MPa) | $C_4$ (MPa) | $C_5$ (MPa) |
| 800.0 | 250.0 | 200.0 | 300.0 | 225.0 |

### A.2. Methodology for identifying material properties from data

The properties needed by the model can be obtained from relatively simple uniaxial experimental data on paper or paperboard pulp material.

#### A.2.1. Elastic constants

The initial elastic behavior is taken to be orthotropic in this model. A total of nine elastic constants are needed to define the orthotropic elasticity: the Young's moduli in MD, CD and ZD, the shear moduli $G_{12}$, $G_{13}$, $G_{23}$ and the Poisson's ratio $v_{21}$, $v_{13}$ and $v_{23}$. These data can be obtained by standard uniaxial stress–strain and corresponding lateral strain vs. axial strain curves.

#### A.2.2. Initial yield and subsequent strain hardening

As discussed in the text, for the yield surface, the sub-surface strengths, $S^i$, are directly related to the uniaxial in-plane yield strengths of the material and the corresponding plastic strain ratios.

To obtain the material properties, consider the case where the uniaxial stress–strain curves for tension in the MD and tension in the CD, compression in the MD and compression in the CD have been obtained. Let $X^{\mathrm{t}}$ denote the yield strength for MD uniaxial tension. For this case, the yield condition expressed in Eq. (7) is reduced to:

$$\sum_{i=\mathrm{I}}^{N}\left[\frac{\chi_i X^{\mathrm{t}} N_{11}^i}{S^i}\right]^{2k}-1=0. \tag{A.1}$$

Furthermore, for uniaxial MD tension, the only non-zero contributions, due to the switching controller, are those for the sub-surfaces I and V, which gives

$$\left[\frac{X^{\mathrm{t}}N_{11}^{\mathrm{I}}}{S^{\mathrm{I}}}\right]^{2k}+\left[\frac{X^{\mathrm{t}}N_{11}^{\mathrm{V}}}{S^{\mathrm{V}}}\right]^{2k}-1=0. \tag{A.2}$$

Similarly, for the case of uniaxial tension in CD, the yield criterion reduces to:

$$\left[\frac{Y^{\mathrm{t}}N_{33}^{\mathrm{II}}}{S^{\mathrm{II}}}\right]^{2k}+\left[\frac{Y^{\mathrm{t}}N_{33}^{\mathrm{IV}}}{S^{\mathrm{IV}}}\right]^{2k}-1=0, \tag{A.3}$$

where $Y^{\mathrm{t}}$ denotes the CD tensile yield strength. For the case of MD compression, the yield condition becomes:

$$\left[\frac{-X^{\mathrm{c}}N_{11}^{\mathrm{II}}}{S^{\mathrm{II}}}\right]^{2k}+\left[\frac{-X^{\mathrm{c}}N_{11}^{\mathrm{IV}}}{S^{\mathrm{IV}}}\right]^{2k}-1=0, \tag{A.4}$$

where $X^{\mathrm{c}}>0$ is the MD compression yield strength. For the case of CD compression:

$$\left[\frac{-Y^{\mathrm{c}}N_{33}^{\mathrm{I}}}{S^{\mathrm{I}}}\right]^{2k}+\left[\frac{-Y^{\mathrm{c}}N_{33}^{\mathrm{V}}}{S^{\mathrm{V}}}\right]^{2k}-1=0, \tag{A.5}$$

where $Y^{\mathrm{c}}>0$ is the CD compression yield strength. Thus, by solving the Eqs. (A.2)–(A.5) for four unknowns, $S^i$, $i=\mathrm{I}$, II, IV and V, direct relations between the $S^i$, $i=\mathrm{I}$, II, IV and V and uniaxial tensile and compressive yield strengths are obtained as follows:

$$S^{\mathrm{I}} = \left(\frac{\Omega_2}{\Omega_1}\right)^{1/2k}; \tag{A.6}$$

$$S^{\mathrm{II}} = \left(\frac{\Omega_4}{\Omega_3}\right)^{1/2k}; \tag{A.7}$$

$$S^{\mathrm{IV}} = Y^{\mathrm{t}} N_{33}^{\mathrm{IV}} \left[1 - (Y^{\mathrm{t}} N_{33}^{\mathrm{II}})^{2k} \left(\frac{\Omega_3}{\Omega_4}\right)\right]^{-1/2k} \tag{A.8}$$

and

$$S^{\mathrm{V}} = X^{\mathrm{t}} N_{11}^{\mathrm{V}} \left[1 - (X^{\mathrm{t}} N_{11}^{\mathrm{I}})^{2k} \left(\frac{\Omega_2}{\Omega_1}\right)\right]^{-1/2k}, \tag{A.9}$$

where

$$\Omega_1 = \left[-Y^{\mathrm{c}} N_{33}^{\mathrm{V}}\right]^{2k} - \left[X^{\mathrm{t}} N_{11}^{\mathrm{V}}\right]^{2k}, \tag{A.10}$$

$$\Omega_2 = (X^{\mathrm{t}} Y^{\mathrm{c}})^{2k} \left[(N_{11}^{\mathrm{I}} N_{33}^{\mathrm{V}})^{2k} - (N_{33}^{\mathrm{I}} N_{11}^{\mathrm{V}})^{2k}\right], \tag{A.11}$$

$$\Omega_3 = \left[-X^{\mathrm{c}} N_{11}^{\mathrm{IV}}\right]^{2k} - \left[Y^{\mathrm{t}} N_{33}^{\mathrm{IV}}\right]^{2k} \tag{A.12}$$

and

$$\Omega_4 = (X^{\mathrm{c}} Y^{\mathrm{t}})^{2k} \left[(N_{11}^{\mathrm{IV}} N_{33}^{\mathrm{II}})^{2k} - (N_{33}^{\mathrm{IV}} N_{11}^{\mathrm{II}})^{2k}\right]. \tag{A.13}$$

The equivalent yield strengths for the two shear sub-surfaces are taken to be equal, $S^{\mathrm{III}} = S^{\mathrm{VI}}$. With one additional experimental stress–strain curve, for example, the in-plane shear MD–CD stress–strain curve which gives the shear strength $Z^{\mathrm{t}}$, $S^{\mathrm{III}}$ (and $S^{\mathrm{VI}}$) can be expressed as a function of $X^{\mathrm{t}}$, $Y^{\mathrm{t}}$, $X^{\mathrm{c}}$, $Y^{\mathrm{c}}$ and $Z^{\mathrm{t}}$ by applying the same method. However, a shear stress–strain curve may be difficult to obtain for paper material. Instead, an off-axis tensile stress–strain curve can be used to calculate $S^{\mathrm{III}}$ and $S^{\mathrm{VI}}$. Here, the uniaxial stress–strain curve in the off-axis direction 45° to the MD direction is used. The uniaxial stress state in the off-axis direction can be transformed to the material directions by a simple tensor rotation which gives the following non-zero stress components instead:

$$\overline{\boldsymbol{T}} = \frac{V^{45}}{2} \begin{bmatrix} 1 & 1 & 0 \\ 1 & 1 & 0 \\ 0 & 0 & 0 \end{bmatrix}, \tag{A.14}$$

where $V^{45}$ is the yield stress obtained from the 45° off-axis stress–strain curve. Substitution of $\overline{\boldsymbol{T}}$ into the yield condition and utilizing the values of $S^i$, $i = \mathrm{I}$, II , IV and V already obtained, $S^{\mathrm{III}}$ and $S^{\mathrm{VI}}$ are related to the in-plane experimental data by:

$$S^{\mathrm{III}} = S^{\mathrm{VI}} = V^{45} N_{13}^{\mathrm{III}} \left[1 - \left(\frac{(V^{45}/2)N_{11}^{\mathrm{I}} + (V^{45}/2)N_{33}^{\mathrm{I}}}{S^{\mathrm{I}}}\right)^{2k} - \left(\frac{(V^{45}/2)N_{11}^{\mathrm{II}} + (V^{45}/2)N_{33}^{\mathrm{II}}}{S^{\mathrm{II}}}\right)^{2k}\right]^{-1/2k}. \tag{A.15}$$

## References


Arcan, M., Hashin, Z., Voloshin, A., 1978. A method to produce uniform plane-stress states with applications to fiber-reinforced materials. Experimental Mechanics 18 (4), 141–146.

Arramon, Y.P., Mehrahadi, M.M., Martin, D.W., Cowin, S.C., 2000. A multidimensional anisotropic strength criterion based on Kelvin modes. International Journal of Solids and Structures 37, 2915–2935.

Castegnade, B., Mark, R.E., Seo, Y.B., 1989. New concepts and experimental implications in the description of the 3-d elasticity of paper. Journal of Pulp and Paper Science 15 (6), 151–159.

deRuvo, A., Carlsson, L., Fellers, C., 1980. The bi-axial strength of paper. TAPPI 63 (5), 133–136.

Dunn, H., 2000. Masters Thesis. Department of Mechanical Engineering, Massachusetts Institute of Technology.

Fellers, C., Westerlind, B., deRuvo, A., 1981. An investigation of the biaxial failure envelope of paper. In: Proceedings of 7th Fundamental Research Symposium: The Role of Fundamental Research in Papermaking, pp. 527–556.

Gunderson, D.E., 1983. Determining paperboard strength. In: International Paper Physics Conference, pp. 253–263.

Gunderson, D.E., Bendtsen, L.A., Rowlands, R.E., 1986. A mechanistic perspective of the biaxial strength of paperboard. ASME Journal of Engineering Materials and Technology 108, 135–140.

Karafillis, A.P., Boyce, M.C., 1993. A general ansiotropic yield criterion using bounds and a transformation weighting tensor. Journal of the Mechanics and Physics of Solids 41 (12), 1886–1895.

Koubaa, A., Koran, Z., 1995. Measure of the internal bond strength of paper/board. TAPPI 78 (3), 103–111.

Mann, R.W., Baum, G.A., Habeger, C.C., 1981. Orthotropic elastic constants of paper. TAPPI 64 (8), 97.

Page, D., Schulgasser, K., 1989. Evidence for a laminate model for paper. In: Mechanics of Cellulose and Polymeric Materials, vol. 99. ASME Applied Mechanics Division, New York, pp. 35–39.

Perkins, R., Sinha, S., 1992. A micromechanics plasticity model for the uniaxial loading of paper materials. In: Plastic Flow and Creep, vol. 135. ASME Applied Mechanics Division, New York, pp. 117–135.

Persson, K., 1991. Material model for paper, Diploma report. Lund Institute of Technology, Lund, Sweden.

Schulgasser, K., Page, D., 1988. The influence of transverse fiber properties on the in-plane elastic behavior of paper. Composite Science and Technology 32, 279–292.

Sinha, S., Perkins, R., 1995. A micromechanics constitutive model for use in finite element analysis. In: Mechanics of Cellulosic Materials, vol. 209. ASME Applied Mechanics Division, New York, pp. 69–89.

Stahl, D.C., Cramer, S.M., 1998. A three-dimensional network model for a low density fibrous composite. ASME Journal of Engineering Materials and Technology 120, 126–130.

Stenberg, N., 2001. Communications between Stenberg and Xia.

Stenberg, N., Fellers, C., Östlund, S., 2001a. Measuring the stress–strain properties of paperboard in the thickness direction. Journal of Pulp and Paper Science 27 (6), 213–221.

Stenberg, N., Fellers, C., Östlund, S., 2001b. Plasticity in the thickness direction of paperboard under combined shear and normal loading. ASME Journal of Engineering Materials and Technology 123, 184–190.

Xia, Q., Boyce, M.C., Parks, D.M. A constitutive model of paperboard deformation and delamination under through-thickness loading, in preparation.